Theor. Comput. Fluid Dyn. (2020) 34:249–270
https://doi.org/10.1007/s00162-020-00532-0

ORIGINAL ARTICLE

Jie Ma · Zhihua Chen · Dawen Xue · Xiaohui Sun

Influences of boattail structures on aerodynamic characteristics of supersonic spinning projectiles

Received: 23 September 2019 / Accepted: 28 April 2020 / Published online: 16 May 2020

Abstract Previous research studies indicate that the proportion of Magnus force at the spinning projectile tail position is very high. Meanwhile, the large mutations of aerodynamic characteristics are found after adding boattail structures. In order to study the influences of boattail structures on aerodynamics of a spinning projectile, a 6.37-diameter long tangential-ogive-cylinder projectile is selected as the original model. Moreover, several boattail configurations are adopted to investigate the effects of boattail structures on the aerodynamics. Numerical simulations with the use of detached eddy simulation method have been performed to study the modification of boattail structure on the surface pressure of the projectile to expose the effects on the aerodynamic characteristics. The reliability of the numerical method has been validated through comparison with experimental data. The numerical results show that the variations of the wake vortex field due to the boattail structures have important influences on the surface pressure and the aerodynamic characteristics. The results provide important observations which can be valuable for design optimization of supersonic spinning projectile.

Keywords Aerodynamics · Magnus effect · Boattail · Spinning projectile

1 Introduction

In order to ensure flight stability, the supersonic projectile needs to fly with high rotation speed. When the spinning projectile or rockets rotate around their longitudinal axis with a certain incident angle, a lateral force perpendicular to the plane of attack is generated, which is known as the Magnus force in ballistics and the moment of force generated by it is called the Magnus moment. In general, the Magnus force can be approximated to the corresponding normal force, but it is not damped on the whole trajectory, so it has an important impact on the dynamic stability of the projectile [1]. Murphy [2] put forward the criterion of dynamic stability of a

Communicated by Sergio Pirozzoli.

J. Ma
School of Mechanical and Power Engineering, Nanjing Tech University, Nanjing 211816, Jiangsu, China

Z. Chen (✉)
National Key Laboratory of Transient Physics, Nanjing University of Science and Technology, Nanjing 210094, Jiangsu, China
E-mail: chenzh@njust.edu.cn

D. Xue
School of Naval Architecture and Ocean Engineering, Zhejiang Ocean University, Zhoushan 316022, Zhejiang, China

X. Sun
Shanghai Aerospace Control Technology Institute, Shanghai 201109, China

spinning projectile. Magnus effect is the main cause of dynamic instability of low-resistance projectiles, and it has become one of important limitations in the design of low-resistance projectiles.

In recent years, with the rapid development of computational fluid dynamics (CFD), many researchers have applied CFD technology to study the flow fields of spinning projectiles. Pechier et al. [3,4] conducted numerical simulation study on the high-speed spinning projectile and rockets. The flow fields are simulated by giving a tangent velocity for projectile surface with the use of Reynolds-averaged Navier–Stokes (RANS) equations and the improved Baldwin–Lomax turbulence model, and the good agreement with experiments was obtained when the angle of attack was $\alpha < 5°$. Silton [5] used the commercial software CFD++ to conduct numerical simulation of the spinning projectile when the Mach number of the incoming flow between 0.7 and 2.7 and the angles of attack are 0°, 2° and 5°. The results of drag and lift coefficients are in good agreement with corresponding experimental values and semi-empirical formulas, but the results of Magnus force and moment are quite different from the experimental values. DeSpirio [6,7] used commercial software CFD++ to conduct the numerical simulations of the flow fields around the spinning projectile (M910) under different Mach numbers and angles of attack of 0, 2°, 3° and 5° incoming flow conditions. The results show that the Magnus force and moment obtained by the RANS and large eddy simulation (LES) hybrid model (RANS/LES) have the best agreement with the experimental values at the subsonic and transonic flow. At the same time, it was found that there is a large percentage of Magus effect around the projectile tail. DeSpirio [8] conducted numerical simulation of the flow field around 7 times diameter spinning projectile. Different from the numerical results of the M910 spinning projectile, with the use of the RANS/LES model, the Magnus moment obtained under the subsonic and transonic flow conditions is larger than the experimental value. It was also found that boattail structure has a gain influence on Magnus effect.

The effects of boattail structures on the aerodynamics of spinning projectiles have also been studied. Silton [9] studied the boattail effect on the bottom resistance at zero incidence angle. DeSpirito [10] studied the influence of boattail shape on spinning stability projectile, and the results showed that boattail structure had a great influence on Magnus effect and dynamic stability. Sturek et al. [11] also studied the influence of boattail shape on the aerodynamic characteristics of supersonic spinning projectile and quantitatively analyzed the variation of Magnus force and moment with the boattail length and angle. LES model can capture and explain the combustion structures of the hydrogen-fueled scramjet combustor with dual cavity very well [12]. The counterrotating vortex structures induced by the injection also can be captured very well with the use of LES model in supersonic combustion flow field with hydrogen injection [13]. Huang et al. [14] investigated the effect of the turbulence model and slot width on the transverse slot injection flow field and found that the RNG k-ε turbulence model could predict the transverse slot injection more accurately for low jet-to-crossflow pressure ratio; meanwhile, the SST k-ω turbulence model was better for the high jet-to-crossflow pressure ratio. Simon et al. [15] improved the accuracy of numerical simulation of projectile wake by optimizing S–A turbulence model and analyzed the wake flow field changes caused by boattail structure. Melissa [16] improved the prediction accuracy of the aerodynamic effect of the boattail by optimizing the Missile DATCOM algorithm.

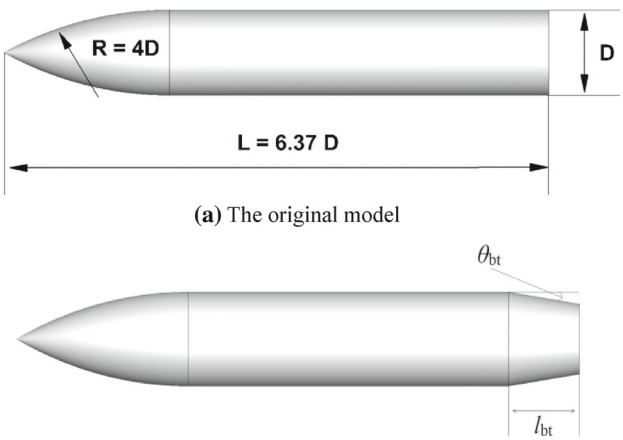

(a) The original model

(b) The new model

Fig. 1 Computational model

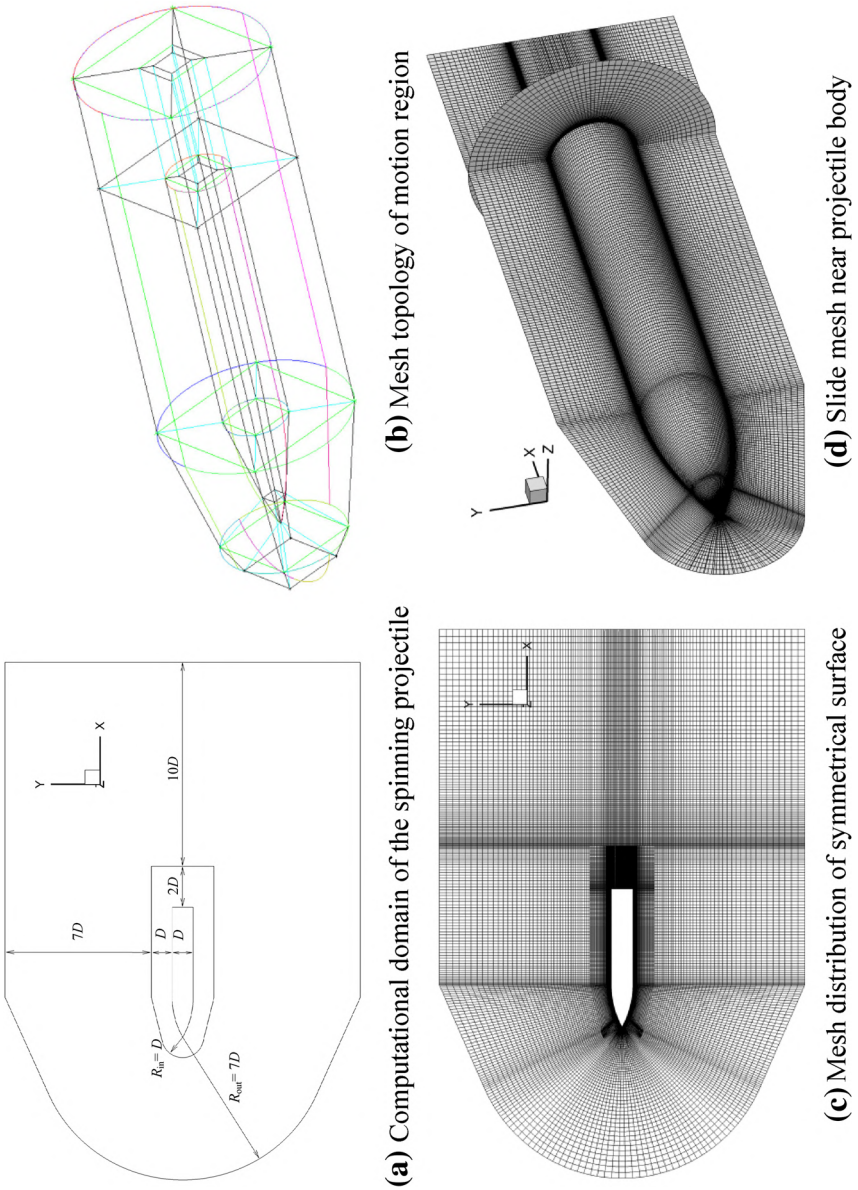

Fig. 2 Schematic diagram of mesh generation

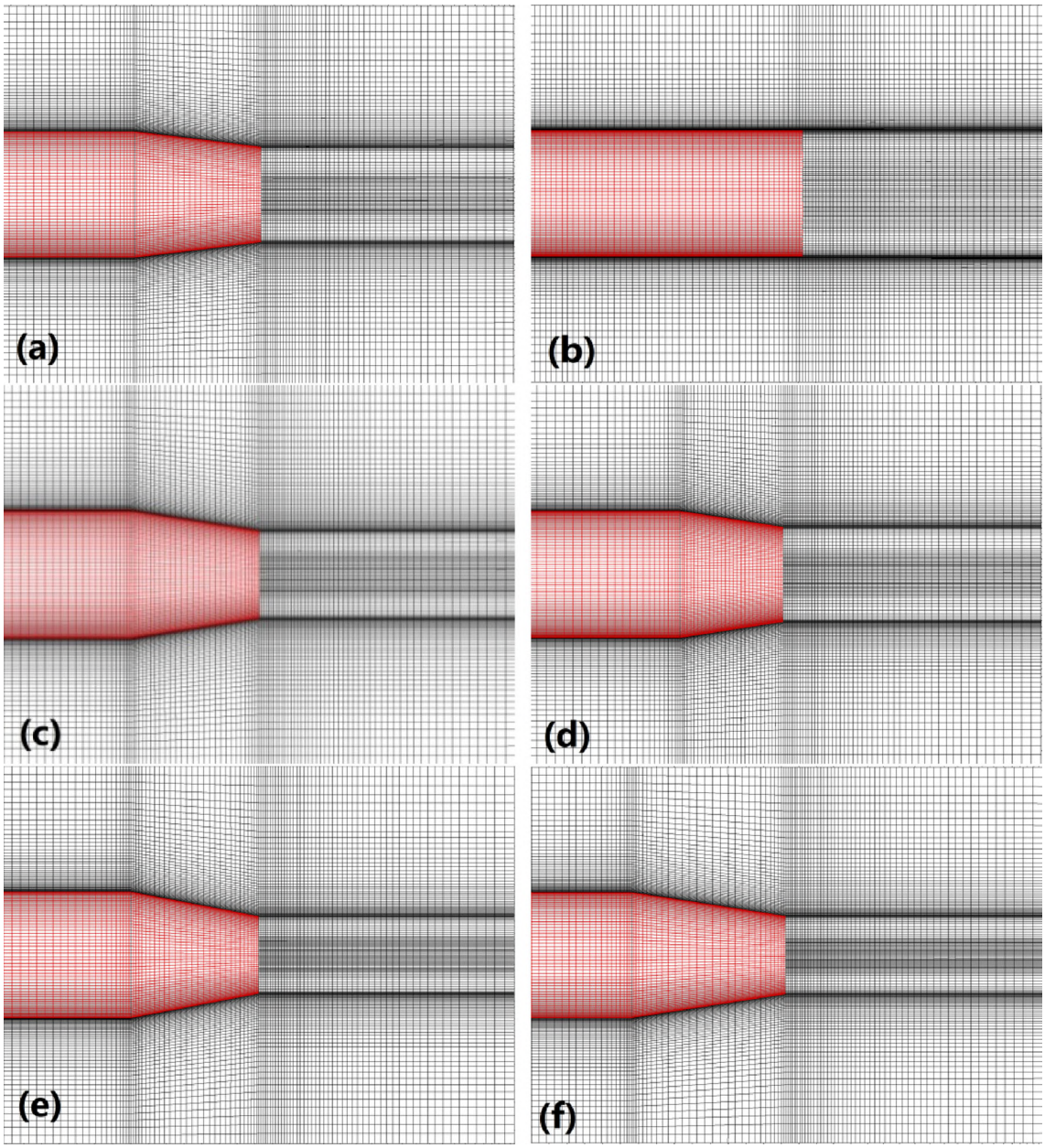

Fig. 3 Partial mesh of several new models with different boattail

However, even previous research results all indicate that the proportion of Magnus force at the boattail position is very high along the axial direction of the spinning projectile [17]. Their researches are basically based on the condition of zero incident angle. Practically, the large mutations of aerodynamic characteristics are found after adding the boattail structure at nonzero incident angle [18]. In order to explain this phenomenon and the potential mechanism of boattail influence on Magnus effect, it is necessary to seek the relation between the coupling effect of projectile wake vortex and asymmetric pressure field. Therefore, the 6.37-diameter long TOC projectile is selected as the original model [17] in this paper. Several boattail configurations are adopted to investigate the effect of boattail structure on aerodynamics. Numerical simulations with the use of DES method [19] have been performed to study the influence of trailing vortex structure on aerodynamics and to explore the effects of base shape on the aerodynamic characteristics of the projectile.

2 Computational approach

In order to study the influence of boattail structure on the aerodynamic characteristics of spinning projectiles, the 6.37-caliber long TOC projectile is selected as original model, which is shown in Fig. 1a. The geometry consists of a tangential-ogive-nose and a 4.43-caliber long cylindrical afterbody. The total length of the TOC projectile is 6.37 diameters ($1D = 30$ mm). Firstly, the comparative analysis of aerodynamic characteristics of the projectile with and without boattail added is carried out. Then, the influence of boattail structure on aerodynamic characteristics of spinning projectile is studied (Fig. 1b), where l_{bt} is the length of the boattail and θ_{bt} represents the boattail angle.

Figure 2a shows the schematic diagram of the computational domain which is divided into external fixed region and internal sliding motion region. Due to the three-dimensional (3D) flow fields, the O-grid generating technology is employed to conduct the division of structured grid. Figure 2b shows the block of inner region through O-grid technology, and Fig. 2c shows the grid diagram of the longitudinal section. The elements near the wall region are refined to ensure $y^+ = 1$ for the viscous boundary layer. In addition, the grid elements are refined at the inflection points to better capture the wave structure in the flow fields. Figure 2d shows the grid distribution near the wall regions. Simply modifying the block at the boattail structure can generate the meshes of several new models for studying the effect of boattail structure on the aerodynamic characteristics, as shown in Fig. 3.

For the numerical simulation, the commercial code ANSYS FLUENT V16.0 was used. After several calculation and comparative analysis, the numerical simulation results of DES method for spinning projectile are the best [20,21], which use LES for the main flow area and the RANS near the wall area. AUSM+ scheme is adopted for capturing shock wave accurately. While the viscous term is discretized with the central difference scheme, the time term is approached using the second-order Runge–Kutta scheme.

In the DES method based on realizable k-ε model, the model equations are shown as follows:

$$\frac{\partial}{\partial t}(\rho k) + \frac{\partial}{\partial x_i}\left(\rho k u_j\right) = \frac{\partial}{\partial x_i}\left[\left(\mu + \frac{\mu_t}{\sigma_k}\right)\frac{\partial k}{\partial x_j}\right] + G_k - \rho\frac{k^{3/2}}{l} \tag{1}$$

$$\frac{\partial}{\partial t}(\rho \varepsilon) + \frac{\partial}{\partial x_j}\left(\rho \varepsilon u_j\right) = \frac{\partial}{\partial x_j}\left[\left(\mu + \frac{\mu_t}{\sigma_\varepsilon}\right)\frac{\partial \varepsilon}{\partial x_j}\right] + \rho C_1 S\varepsilon - \rho C_2\frac{\varepsilon^2}{k + \sqrt{\nu\varepsilon}} \tag{2}$$

where $\mu_t = \rho C_\mu k^{1/2} l$, $C_1 = \max\left[0.43, \frac{\eta}{\eta+5}\right]$, $\eta = S\frac{k}{\varepsilon}$, $S = \sqrt{2S_{ij}S_{ij}}$.

$$l = \min\left(l_{k-\varepsilon}, C_{\mathrm{DES}}\Delta_{\max}\right) \tag{3}$$

where $l_{k-\varepsilon} = \frac{k^{3/2}}{\varepsilon}$ is the turbulence scale parameter in the k-ε turbulence model, $C_{\mathrm{DES}} = 0.61$, $\Delta_{\max}$ is the maximum grid scale in x, y and z directions.

The surface of the projectile is considered as the non-slip wall, and the mesh moves with the projectile. The sliding boundary condition is used for the interfaces between the external fixed area and the internal moving area. The outer boundary adopts the pressure far-field boundary condition, and the incoming flow condition is Mach number $Ma = 3$, total temperature $T_0 = 295$ K, and total pressure $P_0 = 7.41 \times 10^5$ Pa. It can be deduced that static pressure $P_\infty = 20,800$ Pa, static temperature $T_\infty = 106.2$ K, and density $\rho_\infty = 0.682$ kg/m^3. The Reynolds number based on the projectile diameter is $\mathrm{Re} = 1.71 \times 10^6$, the dimensionless rotation speed $\Omega^* = pD/2U_\infty = 0.154$, and the rotation direction is counterclockwise looked from the projectile bottom.

It is essential that the numerical results should be grid-independent to ensure the calculation accuracy. In this paper, the total number of grids ranges from 542,295 to 3041,694 for the original model. Table 1 shows the results of grid independency test. As is shown, the Magnus force coefficient does not change significantly

Table 1 Results of grid independency test

Number of elements	Magnus force coefficient
542,295	− 0.00141895
964,000	− 0.00150432
1,643,227	− 0.001.5431
2,017,298	− 0.00161746
2,490,665	− 0.001.61194
3,041,694	− 0.00161784

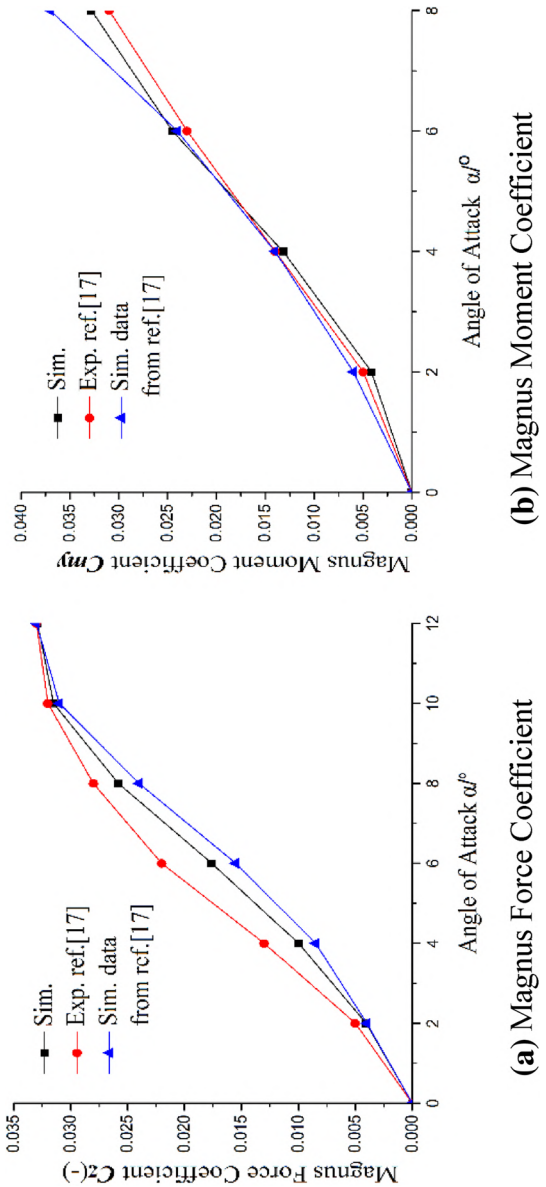

Fig. 4 The measured Magnus coefficients in contrast with the simulated data of the original model at $Ma = 3$

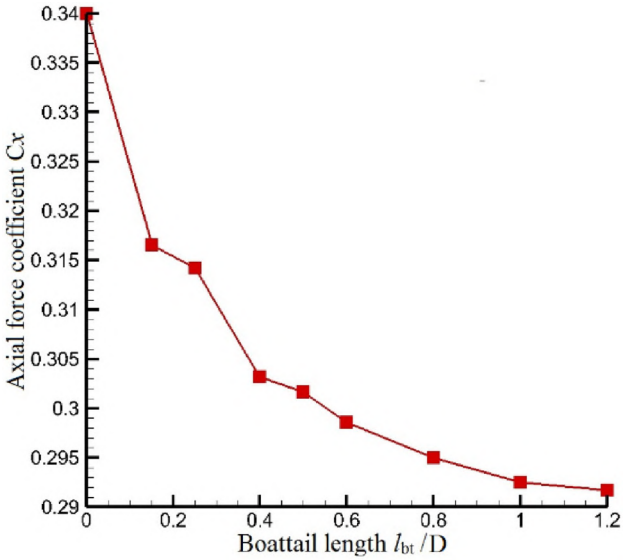

Fig. 5 The axial force coefficient changes with the boattail length at $Ma = 3$, $\alpha = 0°$

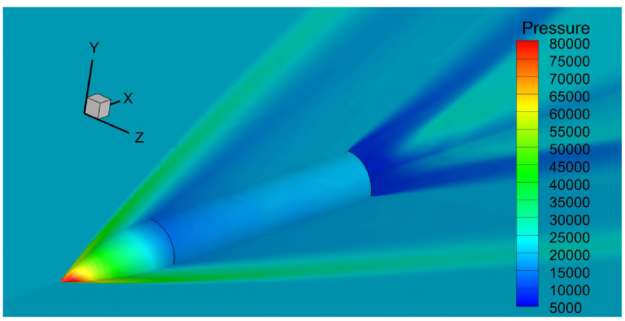

Fig. 6 The pressure distribution of the projectile at $Ma = 3$, $\Omega^* = 0.154$ and $\alpha = 4°$

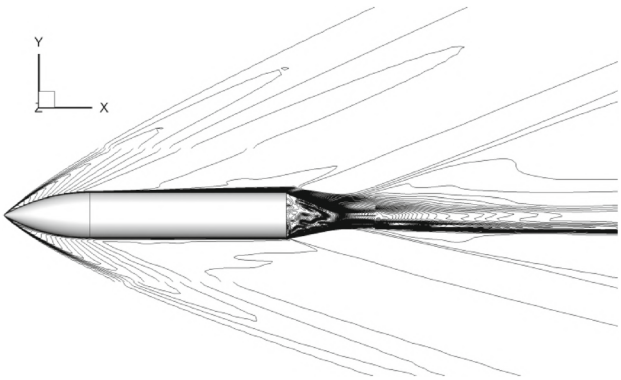

Fig. 7 The corresponding contours of Mach number at $Ma = 3$, $\Omega^* = 0.154$ and $\alpha = 4°$

when the number of grids exceeds 2,017,298. After mesh independence tests, the total number of grids is selected to be 2,490,665.

Figure 4 compares the Magnus force and moment coefficients of our simulation results with the experimental and simulation results of Ref. [17] for a TOC projectile at $Ma = 3$. It can be found that our numerical results agree well with the experimental and numerical data of previous research results in Ref. [17]. Figure 5 shows the relationship between the axial force coefficient and the length of the boattail when $Ma = 3$ and $\alpha = 0°$. With the increase in the boattail length, the axial force (drag) decreases monotonously. However,

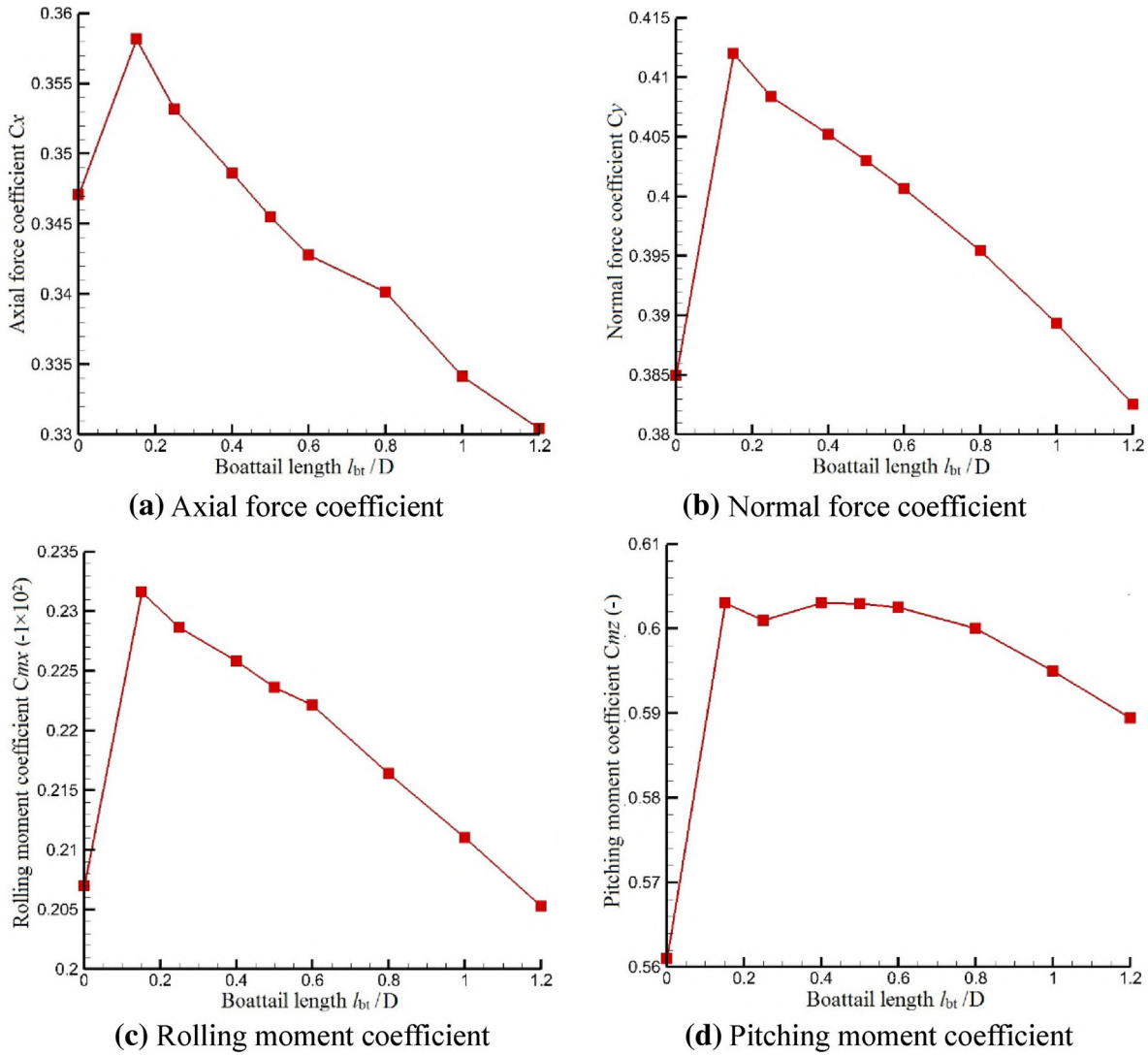

Fig. 8 The variations of aerodynamic coefficients versus the boattail length

for small boattail lengths, its variation gradient becomes large. When the boattail length exceeds 0.8D, the gradient turns into small and gradually becomes constant with the increase in boattail length. And our result also agrees with that of Silton's research [9].

3 Results and discussions

The TOC projectile is chosen to investigate the flow fields. Figure 6 shows the pressure distribution in symmetry plane at the angle of attack, $\alpha = 4°$. Figure 7 shows the corresponding contours of Mach number in plane *xoy*. It is clear that surface boundary layer is thin at the high-pressure area which is the windward side of the projectile, and the thickest boundary layer is found at the boattail.

3.1 Effect of boattail length on aerodynamics at $\alpha = 6°$

Figures 8 and 9 show the variations of aerodynamic coefficients versus the boattail length under the condition of $Ma = 3$ and $\alpha = 6°$. It is clear that, for a large angle of attack ($\alpha = 6°$), the small length ($0.15D$) of boattail structure increases the drag and lift coefficients rapidly; then, a further increase in its length has the opposite

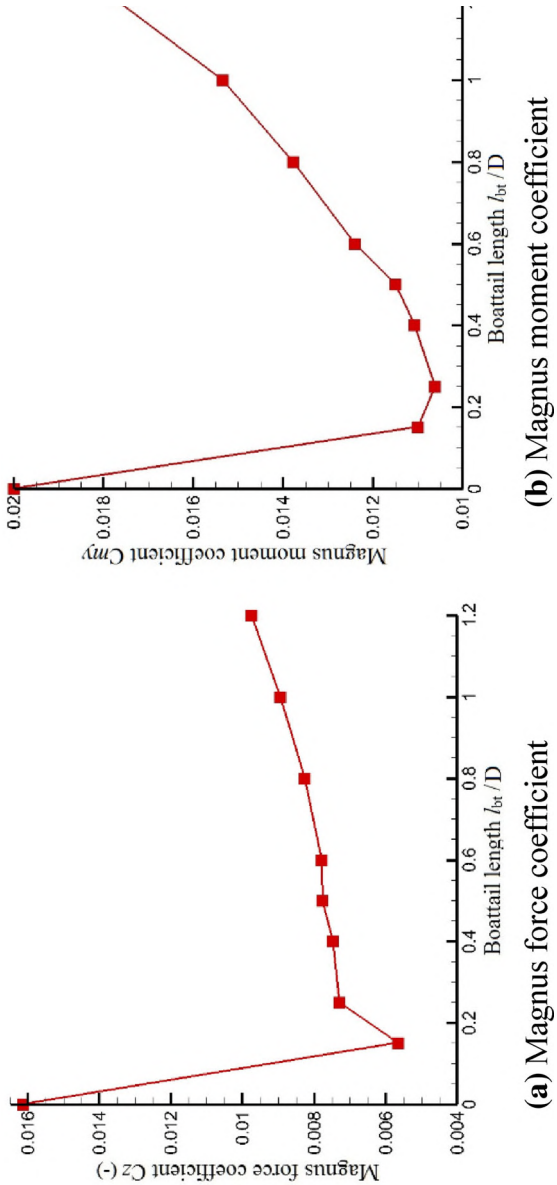

Fig. 9 The variations in Magnus coefficient versus the boattail length

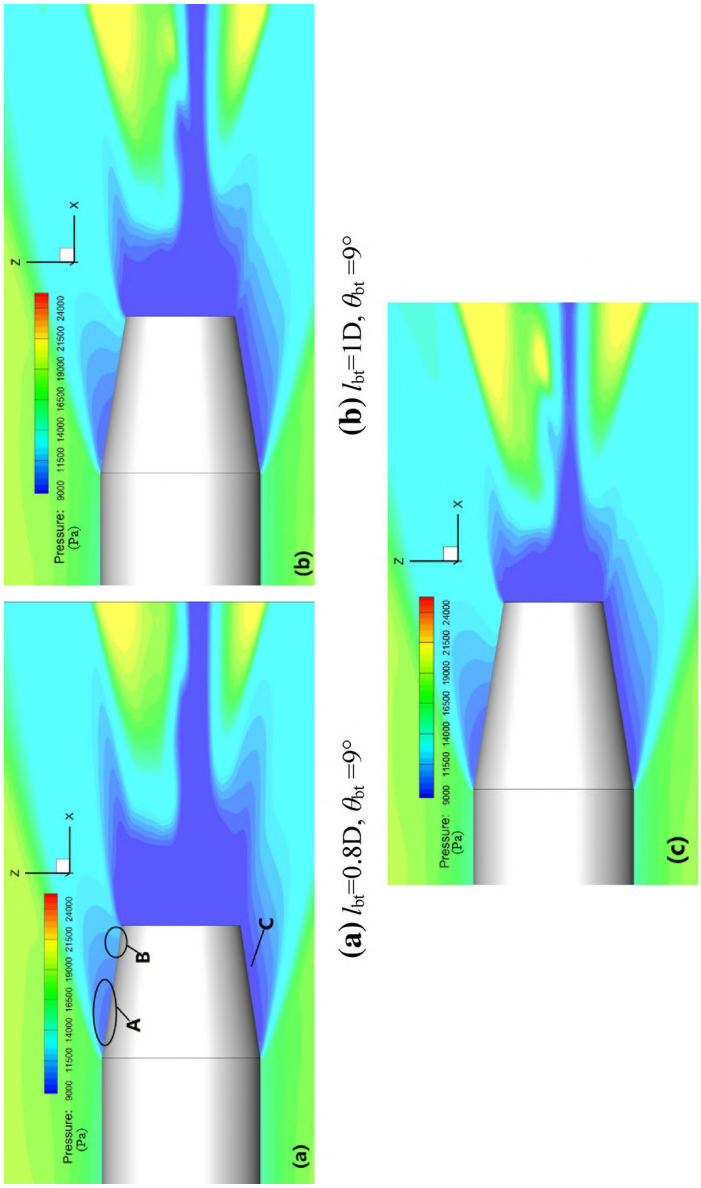

(a) l_{bt}=0.8D, θ_{bt} =9° **(b)** l_{bt}=1D, θ_{bt} =9°

(c) l_{bt}=1.2D, θ_{bt} =9°

Fig. 10 The pressure contour around boattail part under three different boattail lengths

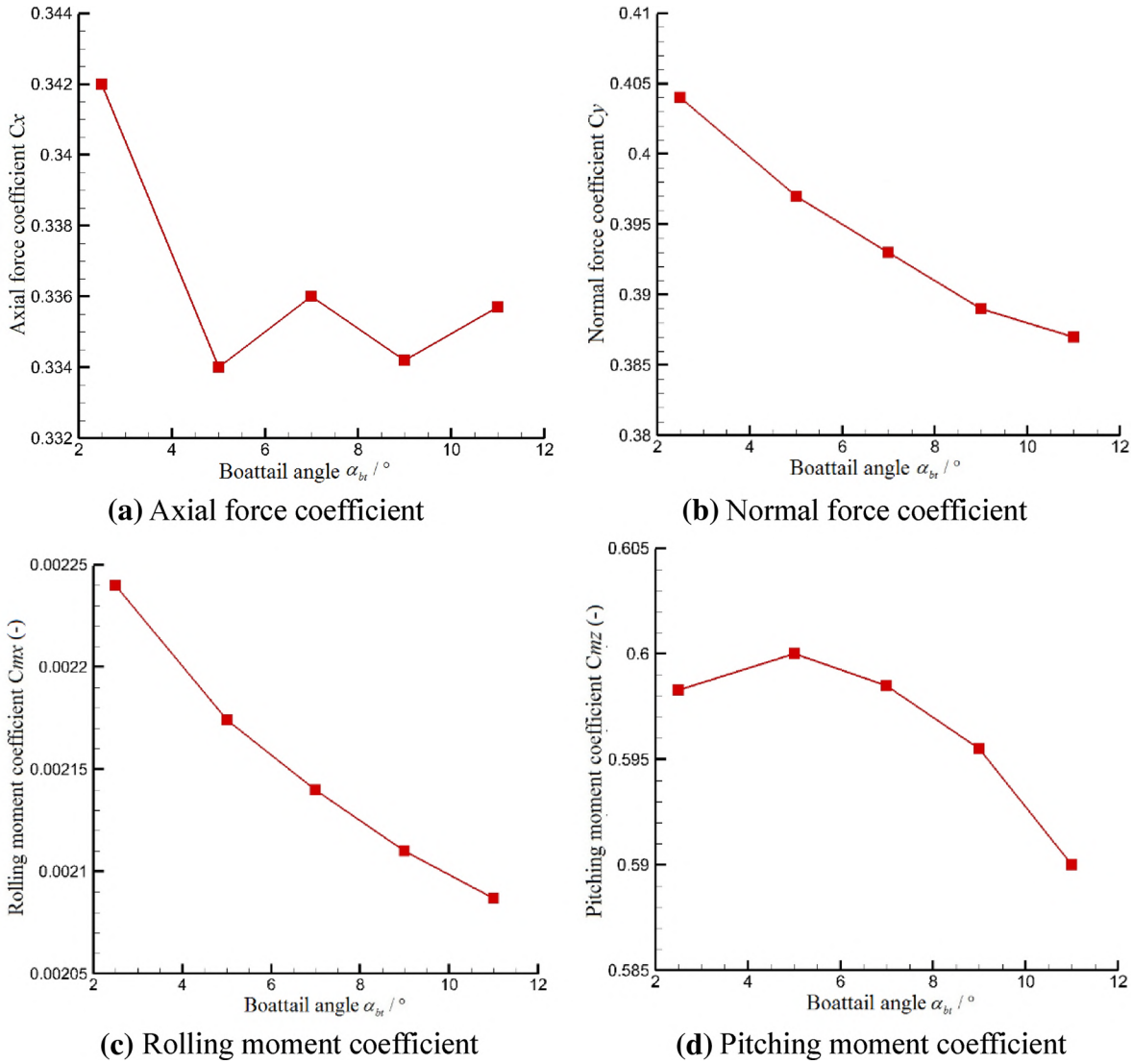

Fig. 11 The variations of aerodynamic coefficients versus the boattail angle

effect, which means decreasing the drag and lift. The drag coefficient will be lower than that of original model when the boattail length is greater than $0.45D$ (Fig. 8a). Meanwhile, the lift coefficient is greater than that of the original model before the boattail length is less than $1.1D$ (Fig. 8b). And the rolling moment has the same variation tendency with that of drag force (Fig. 8c), which increases significantly and then decreases monotonically. Figure 8d shows that the pitching moment coefficient also increases quickly firstly, and stays around 0.6 as the boattail length between 0.15 and $0.8D$, then decreases when boattail becomes larger than $0.8D$, which is beneficial to improve the static stability of the spinning projectile.

Figure 9 shows the variation of Magnus coefficients versus the boattail length. As shown in Fig. 9a, the Magnus force coefficient decreases significantly with $l_{\mathrm{bt}} = 0.15\,D$ and then increases with the raise in the boattail length. Figure 9b shows that the Magnus moment coefficient also has the same variation tendency. After $l_{\mathrm{bt}} \geq 0.6\,D$, Magnus coefficient basically presents linear modification versus boattail length.

Figure 10 displays the pressure contour around boattail part under three different boattail lengths with the boattail angle $\theta_{\mathrm{bt}} = 9°$. It can be seen that the flow structures of the low-pressure area C in three cases are similar due to the same boattail angle. The flow fields behind the first expansion on the $Z+$ side (with positive Z value) are basically the same, so the pressure values in the A zone are almost the same. However, the pressure value in the B zone is relatively large, which ultimately leads to an increase in the Magnus force and the Moment coefficients. According to the comprehensive results, Magnus force and moment tend to increase

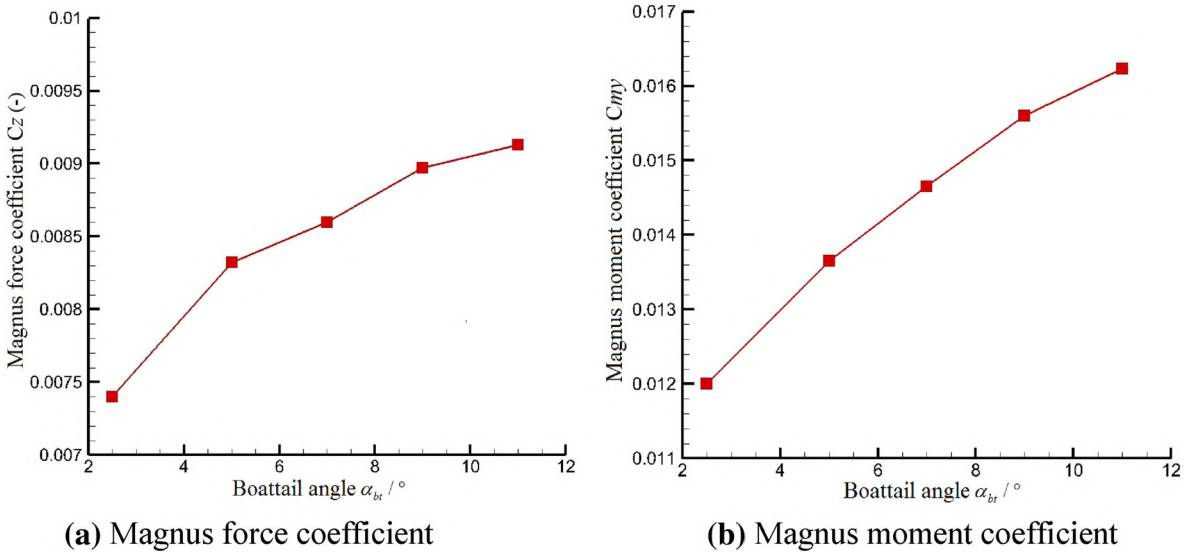

(a) Magnus force coefficient **(b)** Magnus moment coefficient

Fig. 12 The variations of Magnus coefficient versus the boattail angle

with the raise in boattail length. However, compared with the original projectile without boattail structure, Magnus force and moment coefficients are still much smaller. Therefore, boattail structure is conducive to aerodynamic optimization of the spinning projectile.

3.2 Effect of boattail angle on aerodynamics at $\alpha = 6°$

Figures 11 and 12 show the aerodynamic coefficients of the spinning projectile versus the boattail angle θ_{bt} with $Ma = 3$ and $\alpha = 6°$. It can be seen that the drag coefficient fluctuates slightly after the boattail angle $\theta_{bt} = 5°$. The lift and rolling moment coefficient both show a decreasing trend with the increase in the boattail angle. Figure 11d shows that the pitching moment coefficient first increases and then decreases, and there is a maximum value at the $\theta_{bt} = 5°$ position. For the spinning projectile, the smaller pitching moment coefficient is better for the static stability. Combined with the drag coefficient, the boattail angle between 5° and 10° is more reasonable.

Figure 12 shows the Magnus force and moment coefficients versus the boattail angle θ_{bt}. As it shows that both Magnus force and moment coefficients show the increasing trend with the increase in θ_{bt}, but they are much smaller than those of the original projectile with non-boattail. Figure 13 shows the pressure contour around boattail part under three cases of different boattail angles when the boattail length is $l_{bt} = 1D$. It can be seen that the low-pressure area of the expansion wave structure expands with the increase in the boattail angle, making A zone expands and its pressure decreases, and the high-pressure B zone gradually shrinks. With the increase in the boattail angle, the boattail surface on $Z-$ side (with negative Z value) is close to the wake vortex structure, leading to a significant decrease in pressure in C zone, which eventually leads to an increasing trend of Magnus force and moment. Therefore, it can be concluded that the Magnus force and moment tend to raise with the increase in the boattail angle θ_{bt}.

According to the comprehensive results, it is reasonable to choose the range of 7°–10° for the boattail angle of the spinning projectile, which is consistent with the present conventional spinning projectile.

3.3 Influence mechanism of boattail structure on aerodynamic characteristics

The presence or absence of boattail structure has a great impact on aerodynamic force. From the original model with non-boattail to the addition of $0.15D$ boattail, a jump change of aerodynamic coefficients occurs, which is completely different from the monotonic change of the aerodynamic coefficients at angle of attack $\alpha = 0°$. Therefore, it is necessary to further explore the mechanism.

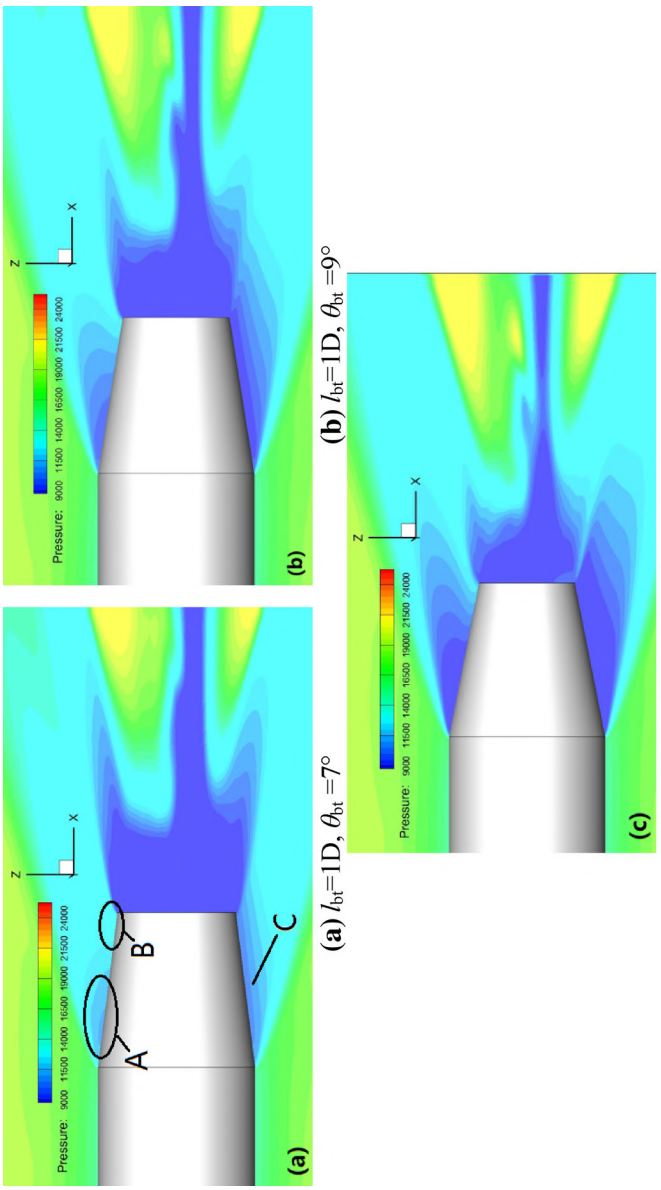

(a) l_{bt}=1D, θ_{bt} =7° **(b)** l_{bt}=1D, θ_{bt} =9° **(c)** l_{bt}=1D, θ_{bt} =11°

Fig. 13 The pressure contour around boattail part under three different boattail angles

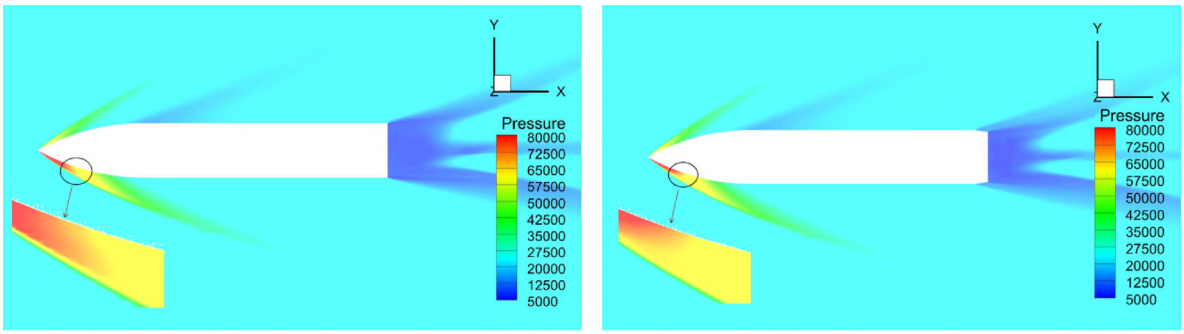

(a) The original projectile with non-boattail **(b)** The projectile with boattail of l_{bt}=0.25D, θ_{bt}=9°

Fig. 14 The pressure distribution on the plane of *xoy* under the condition of $Ma = 3$ and $\alpha = 6°$

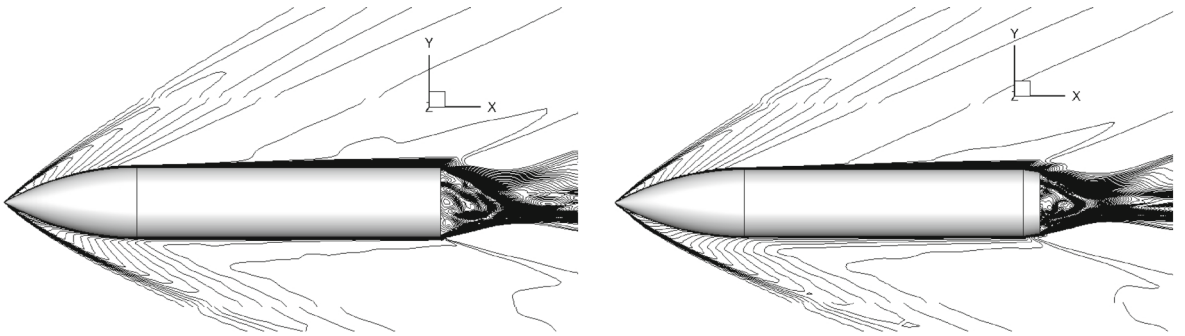

(a) The original projectile with non-boattail **(b)** The projectile with boattail of l_{bt}=0.25D, θ_{bt}=9°

Fig. 15 The instantaneous Mach number contours under the condition of $Ma = 3$ and $\alpha = 6°$

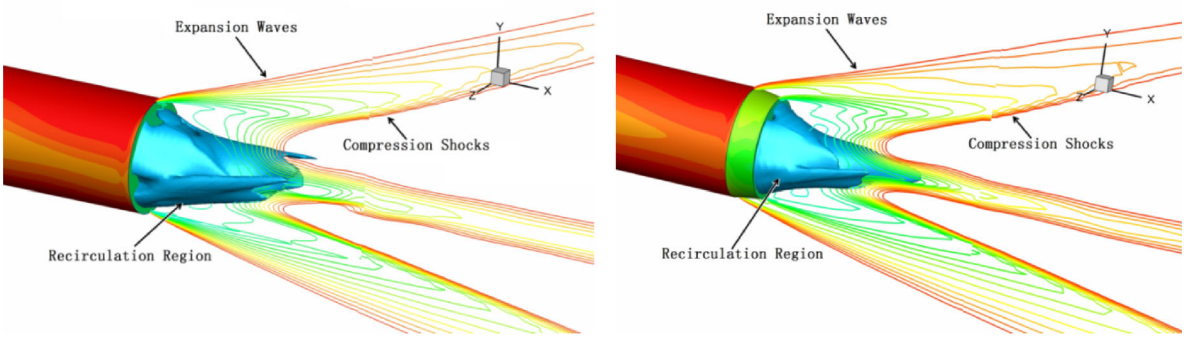

(a) The original projectile with non-boattail **(b)** The projectile with boattail of l_{bt}=0.25D, θ_{bt}=9°

Fig. 16 The instantaneous wake structure of the projectile under the condition of $Ma = 3$ and $\alpha = 6°$

Firstly, the projectile with the boattail structure of $l_{bt} = 0.25D$, $\theta_{bt} = 9°$ is selected as typical example to compare with the original projectile with non-boattail. Figure 14 shows the pressure distribution on the plane of xoy under the condition of $Ma = 3$ and $\alpha = 6°$. Figure 15 shows the instantaneous Mach number contours of two kinds of projectiles. As seen from Fig. 14, the overall flow field structures of the two projectiles are similar, but the pressure distribution in the circular area of the warhead site and the tail position of the projectile is slightly different. The pressure difference of wake field is easy to understand, because it changes from a primary expansion wave to two expansion waves (as shown in Fig. 16). The mechanism for the evolution of the high-pressure area on the warhead is relatively complex. In Fig. 15, the velocity near the windward side increases due to the change in the boattail structure. As a result, the stagnation zone on the windward side of the warhead extends backward, leading the high-pressure aero to expand. Therefore, the drag and lift coefficients of the projectile increase with the addition of boattail structure. From Figs. 14 and 15, the Mach number and

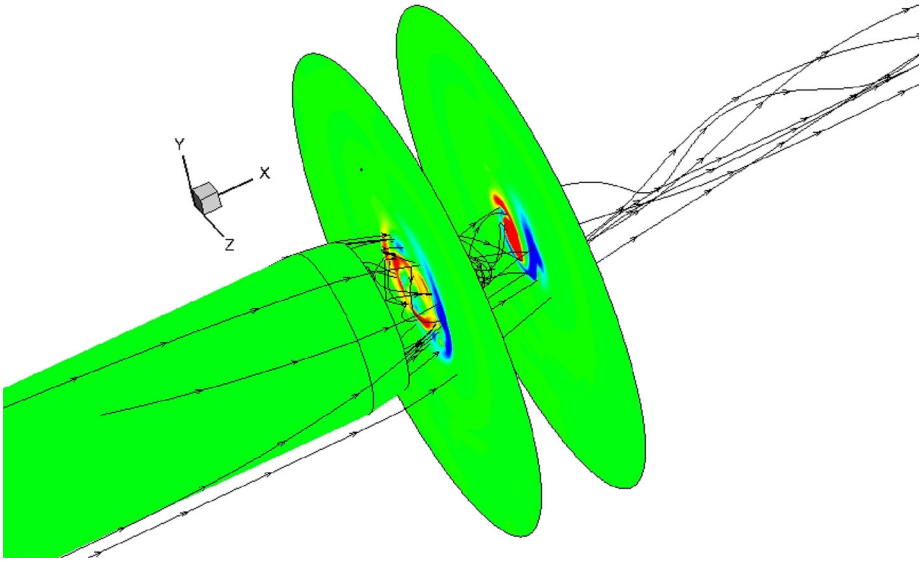

Fig. 17 The instantaneous vorticity and streamline diagram of the wake region as $l_{bt} = 0.25D$, $\theta_{bt} = 9°$

pressure contour on the leeward side are basically the same, and the flow field around leeward side is not affected much.

Figure 17 shows the instantaneous vorticity contour and streamline diagram around wake region when the boattail length is $l_{bt} = 0.25D$ and the boattail angle $\theta_{bt} = 9°$. It can be seen that there is a pair of reverse vortexes in the wake region, and the intensity of the vortex on the $Z-$ side is significantly larger than that on the other side, and its vortex range occupies almost the entire bottom of the projectile. Due to the existence of the asymmetric vortex structure, the velocity around boattail is asymmetrical, and the x direction flow velocity near the $Z-$ side will be faster than the $Z+$ side (Fig. 17). As a result, the pressure value distributed on the $Z-$ side is low and a lateral force (i.e., Magnus force) is formed, which can reasonably explain why the Magnus force on the boattail position is relatively large.

3.3.1 Influence of boattail length on surface pressure distribution

Figure 18 shows the pressure distribution of leeward side and windward side of the projectile with different boattail length ($\theta_{bt} = 9°$). As shown in Fig. 18a, the pressure on the windward side increases with the boattail structure, while the pressure on the leeward side remains basically unchanged, which is consistent with the previous analysis, leading to the increase in lift force. Figure 18b shows the pressure distribution around the boattail. The pressure on the leeward side near the bottom is larger than that on the windward side, and the pressure difference between the leeward side and the windward side gradually increases with the increase in the boattail length. It can conclude that the lift coefficient will decrease with the increase in the boattail length. According to the comprehensive results, the pressure on the windward side increases due to the influence of the addition of the boattail structure, causing a jump in the lift coefficient. As the length of the boattail increases, the additional reverse lift generated by boattail will increase, leading to the gradual decrease in the lift coefficient.

Figure 19 shows the pressure distribution of $Z-$ side and $Z+$ side of the projectile with different boattail lengths ($\theta_{bt} = 9°$). It can be seen that the pressure difference close to the projectile bottom between two sides is very large under the influence of the asymmetric vortex structure of the wake flow, but gradually decreases with the distance away from the bottom. It indicates that Magnus force has a large proportion around the boattail and is obviously affected by wake flow. After the addition of the boattail structure, the pressure difference between two sides decreases significantly due to the barrier effect of the secondary expansion discontinuity formed by the boattail structure, and the upstream affected area is also significantly shortened. However, as shown in Fig. 19b, the boattail structure will generate additional Magnus force while obstructing the upstream influence of wake flow and gradually increase with the raise in the boattail length; therefore, the boattail structure should not be too long.

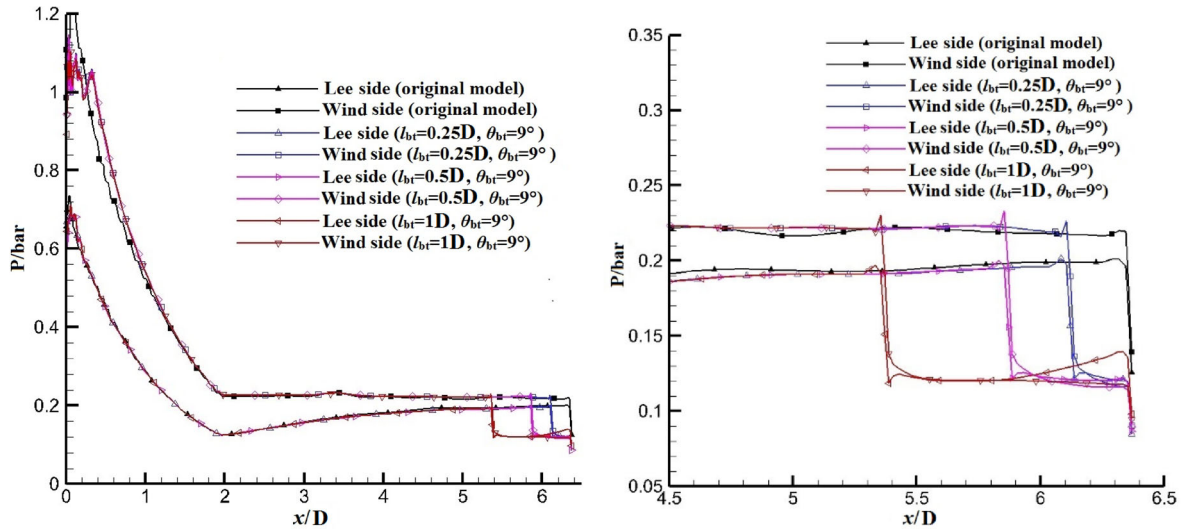

(a) Leeward side and windward side **(b)** Leeward side and windward side of boattail part

Fig. 18 Pressure distribution of leeward side and windward side on the projectile surface

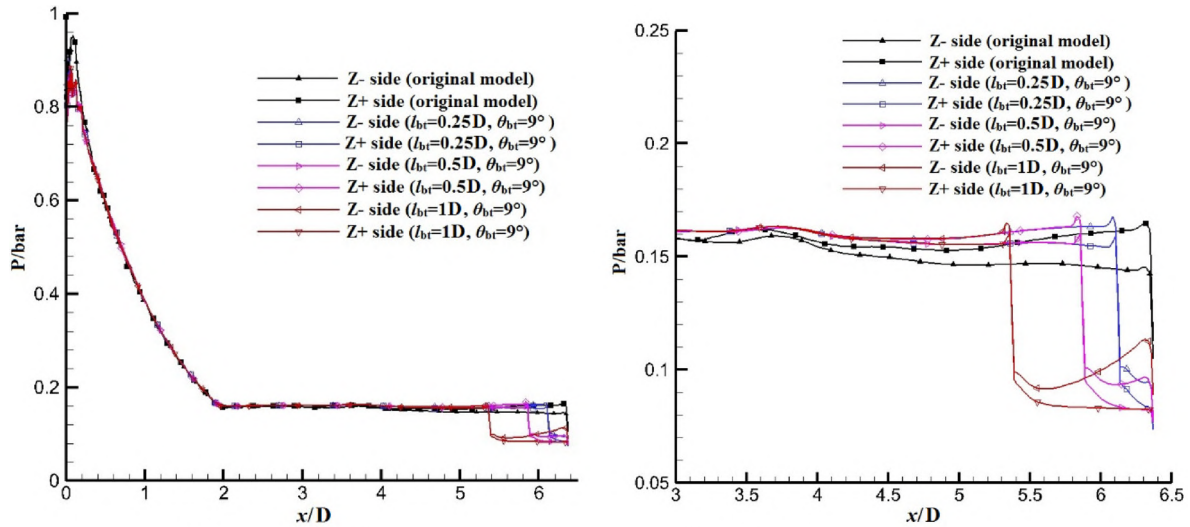

(a) Z- and Z+ side **(b)** Z- and Z+ side of after body part

Fig. 19 Pressure distribution of Z- and Z+ side on the projectile surface

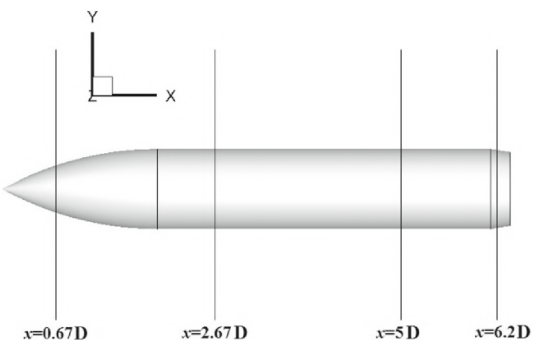

Fig. 20 The location of the cross section *yoz*

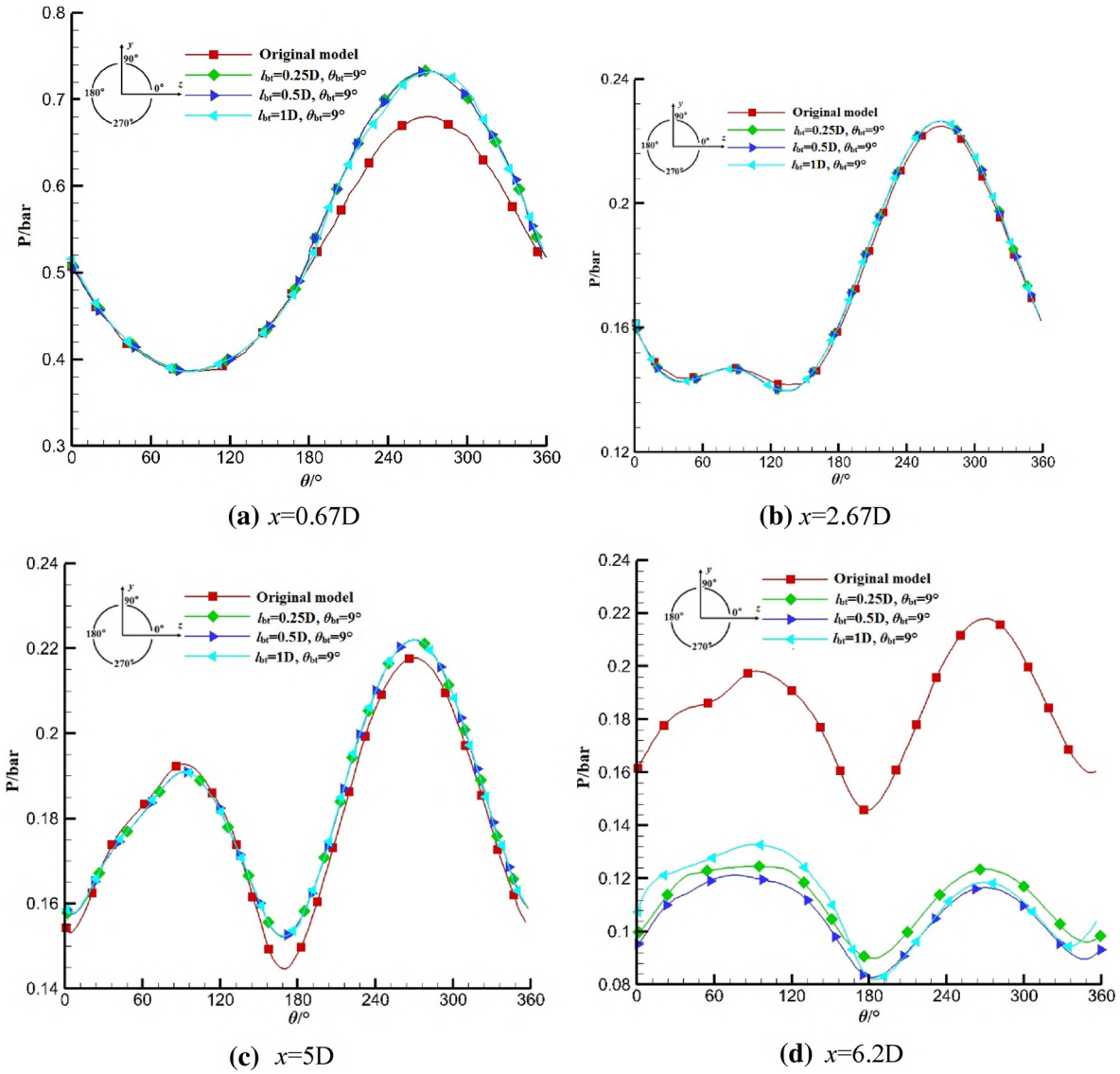

Fig. 21 Circumferential pressure distribution on the projectile surface

In order to further analyze the influence of the boattail structure on the surface pressure distribution, four sections were selected along the projectile axis, respectively $x/D = 0.67$, 2.67, 5 and 6.2, as shown in Fig. 20. Figure 21 displays the circumferential pressure distribution on the surface of the four positions. Figure 21a shows the circumferential pressure distribution on the projectile surface at the warhead ($x = 0.67D$). It can be clearly seen that the pressure distribution on the windward side increases significantly after adding the boattail structure, while the leeward side remains basically unchanged, leading to the increase in lift, which is consistent with the previous analysis. Figure 21b shows the circumjacent pressure distribution on the front of the cylinder ($x = 2.67D$). It can be inferred that a pair of vortex structures form behind the projectile shoulder from the "W"-shaped pressure distribution on the leeward surface. From the deviation of the minimum positions on both sides, it can be known that the vortex structures shift to the smaller θ due to the influence of the boattail structure. From the pressure change of the leeward side, the boattail structure increases the lateral force along the z-negative direction at this position. However, from the side of the windward side, the pressure value on the $Z-$ side increases, and the basic position of the pressure on the $Z+$ side does not change, forming a lateral force in the z-positive direction. In general, the pressure difference formed on the windward side is large, making the Magnus force become smaller, but the change in boattail length has little effect on the pressure distribution. Figure 21c shows the circumferential pressure distribution on the back of the cylindrical section ($x = 5D$)

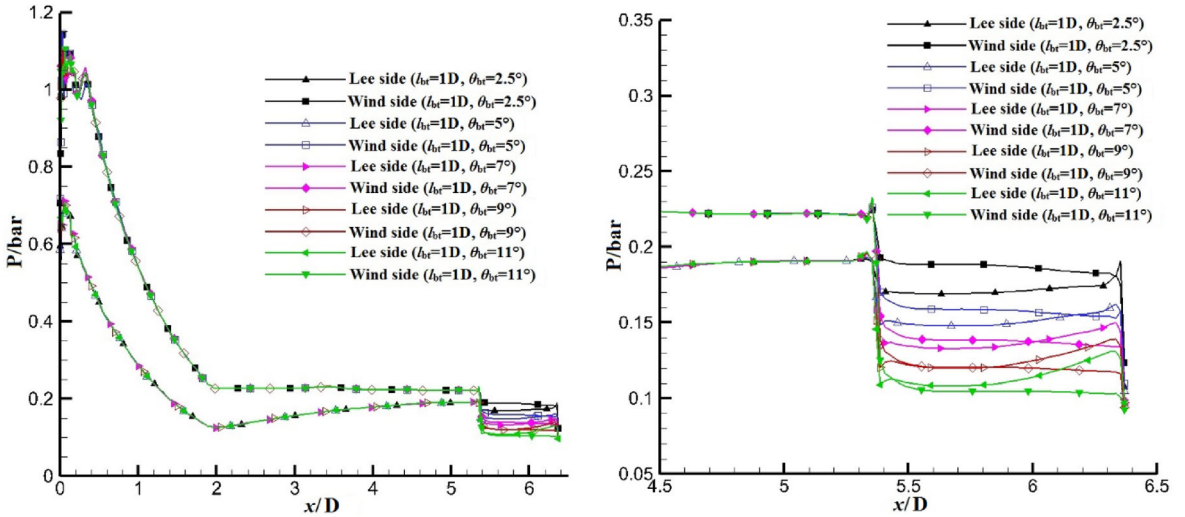

(a) Leeward side and windward side **(b)** Leeward side and windward side at boattail part

Fig. 22 Pressure distribution of leeward side and windward side on the projectile surface

of the projectile (presenting the "M" shape). Compared with the front section of the projectile, the surface pressure distribution of back changes largely. Since the boattail structure effectively weakens the influence of the wake vortex structure on the flow field at this position, two minimum points can be found to increase significantly. The pressure value on the $Z-$ side increases significantly, while that on the $Z+$ side decreases correspondingly, leading to the reduction in Magnus force, which is conducive to the flight stability of the spinning projectile. Figure 21d shows the circumferential pressure distribution at the boattail ($x = 6.2D$), where the pressure distribution changes significantly with the boattail length. Firstly, the position is affected by the expansion wave, which causes the pressure to be significantly smaller than original projectile. Secondly, the pressure value of the leeward side is greater than the pressure of the windward side, so the increase in the boattail length will inevitably lead to the decrease in the lift. It is not difficult to see that there is a minimum value at $\theta = 360°$, and the position of the minimum value moves forward with the increase in the boattail length, and the minimum value is significantly larger than that at $\theta = 180°$. Moreover, the larger the boattail length, the greater the difference between the two minimum values (more apparent from Fig. 19b), so the Magnus force at this position increases when the boattail length increases.

In general, the addition of boattail structure has a great impact on the surface pressure distribution due to the barrier effect of expansion wave discontinuity generated at the junction of boattail and cylindrical section, which can improve lift force and reduce Magnus force. The boattail section is obviously affected by the wake vortexes, and the pressure distribution at the boattail changes greatly versus boattail length. As a result, the lift will gradually decrease and the Magnus force will gradually increase with the raise in the boattail length.

3.3.2 Influence of boattail angle on surface pressure distribution

Figure 22 shows the pressure distribution of leeward side and windward side of the projectile with different boattail angles ($l_{bt} = 1D$). It can be found from Fig. 22a that the boattail angle has little effect on the surface pressure distribution of the projectile except the boattail section. Figure 22b shows the pressure distribution at the boattail, and the windward pressure is greater than the leeward pressure when $\theta_{bt} = 2.5°$, but the leeward pressure appears to be greater than the windward pressure near the projectile bottom. Moreover, the region gradually expands with the increase in θ_{bt}. For $\theta_{bt} \geq 9°$, the leeward pressure of the entire boattail section is larger than windward pressure. It can be concluded that the additional reverse lift generated by the boattail will increase with the raise in the boattail angle θ_{bt}, resulting in the lift coefficient gradually decreasing with the increase in θ_{bt}.

Figure 23 shows the pressure distribution of $Z-$ side and $Z+$ side of the projectile with different boattail angles ($l_{bt} = 1D$). It can be seen from Fig. 23a that the influence of the boattail angle on the surface pressure distribution of the projectile is mainly concentrated on the boattail section. However, the pressure difference between the $Z-$ side and $Z+$ sides gradually increases with the raise in θ_{bt}, and the pressure difference

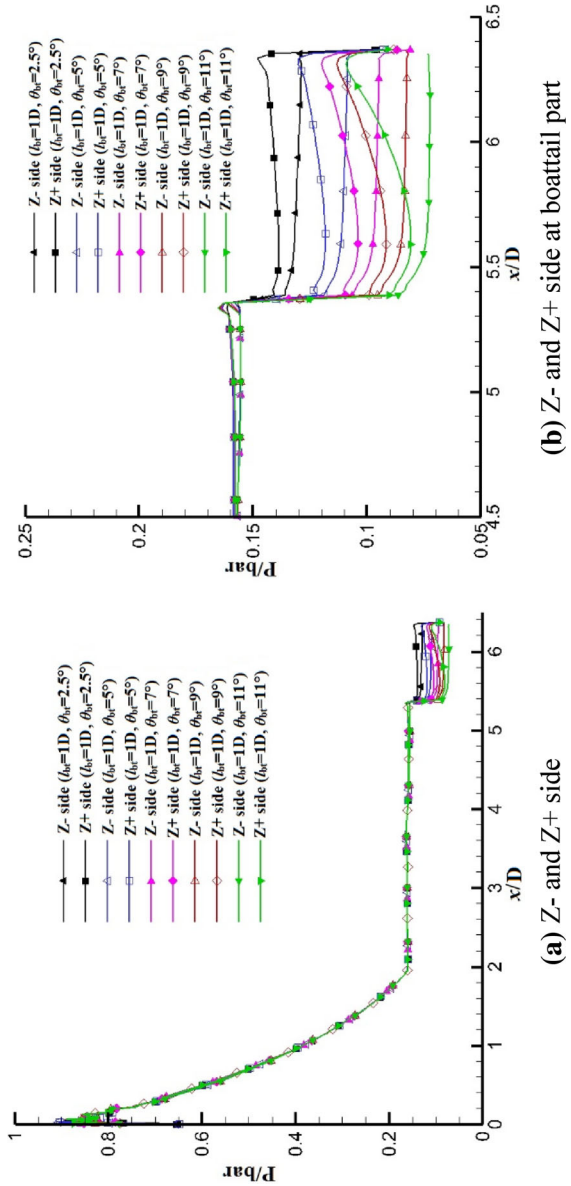

Fig. 23 Pressure distribution of $Z-$ and $Z+$ side on the projectile surface

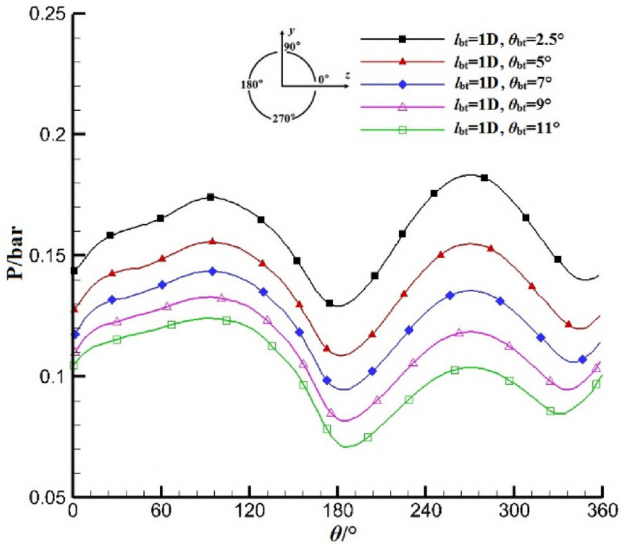

Fig. 24 Circumferential pressure distribution on the projectile surface at cross section of $x = 6.2D$

increases as it is closer to the projectile bottom. It can be concluded that the additional Magnus force generated by the boattail structure will gradually increases with the raise in the boattail angle θ_{bt}, so the boattail should not be too large.

Figure 24 shows the circumferential pressure distribution of the boattail section ($x = 6.2D$), which is affected by the expansion wave. And the intensity of the expansion wave increases with the raise in θ_{bt}, resulting in a decrease in the surface pressure at the position. In addition, it can be seen from the figure that when θ_{bt} is small, the surface pressure of the windward surface is greater than leeward surface. However, as the θ_{bt} increases, the gradient of pressure on the leeward surface is much smaller than windward surface. When $\theta_{bt} = 5°$, the maximums of pressure on both windward side and leeward side are substantially equal. When $\theta_{bt} \geq 5°$, the pressure on the leeward side will be greater than the windward side, resulting in additional reverse lift. Besides, the minimum points between 180° and 360° draw close to 270° with the increase in θ_{bt} on the windward side, and the high-pressure area shrinks, which causes the lift coefficient of the projectile to gradually decrease. The minimums of pressure on the $Z+$ side are significantly larger than the minimums value on the $Z-$ side, and the pressure differences are gradually enlarged with the increase in θ_{bt}. Combined with Fig. 23b, it can be seen that the Magnus force will gradually increase with the increase in θ_{bt}.

4 Conclusion

The 6.37D long TOC projectile is selected as the original model, and several boattail configurations are adopted to investigate the effect of boattail structure on aerodynamics. Numerical simulations with the use of DES method have been performed to study the modification of trailing vortex structure on the surface pressure of the projectile to expose the effects on the aerodynamic characteristics. Based on our numerical results, the conclusions are shown as follows.

(1) After the addition of the boattail structure, the drag, lift and rolling moment coefficients increase substantially and then show a monotonic decreasing law with the increase in the boattail length. The pitching moment coefficient decreases significantly at first and stays around 0.6 as boattail length between $0.15D$ and $0.8D$ and then presents a decreasing law after boattail being larger than $0.8D$.
(2) The Magnus force and moment coefficients decrease significantly after the addition of boattail structure and then increase with the raise in the boattail length.
(3) The drag coefficient fluctuates slightly after the boattail angle $\theta_{bt} = 5°$. The lift coefficient and rolling moment coefficient both show a decreasing trend with the increase in the boattail angle. The pitching moment coefficient first increases and then decreases, and there is a maximum value at the $\theta_{bt} = 5°$ position.

(4) Both Magnus force and moment coefficients show an increasing trend with the raise in θ_{bt}, but they are much smaller than those of the original projectile with non-boattail.
(5) There is a pair of reverse vortexes in the wake region, and the intensity of the vortex on the $Z-$ side is significantly larger than that on the other side, and its vortex range occupies almost the entire bottom of the projectile which results in that the Magnus effect on the boattail position is relatively large.
(6) The addition of boattail structure has a great impact on the surface pressure distribution due to the barrier effect of expansion wave discontinuity generated at the junction of boattail and cylindrical section, which can improve lift force and reduce Magnus force. The boattail section is obviously affected by the wake vortexes, and the pressure distribution at the boattail changes greatly with the versus boattail length. As a result, the lift will gradually decrease and the Magnus force will gradually increase with the raise in the boattail length.
(7) The additional reverse lift generated by the boattail increases with the raise in the boattail angle, resulting in the lift coefficient gradually decreasing with the increase in boattail angle. And, the additional Magnus force generated by the boattail structure gradually increases with the raise in the boattail angle; therefore, it should not be too large.
(8) According to the change trend of the overall aerodynamic coefficients, the reasonable interval of the boattail length of a general projectile is $0.8D$–$1.2D$, and the reasonable interval of the boattail angle is 7°–10°.

Acknowledgements This work was supported by the Introduce Talent Funding for Scientific Research at Nanjing Tech University (Grant No. 39802118).

References

1. Graff, G.Y., Moore, F.G.: Empirical method for predicting the magnus characteristics of spinning shells. AIAA J. **15**(10), 1379–1380 (1977)
2. Murphy, C.H.: Influence of moving internal parts on angular motion of spinning projectiles. J. Guid. Control Dyn. **1**(2), 151–161 (1978)
3. Pechier, M., Guilen, P.: A combined theoretical experimental investigation of magnus effects. In: 16th AIAA Applied Aerodynamics Conference, Chatillon, France, AIAA 98-2797 (1998)
4. Pechier, M., Guillen, P.: Magnus effect over finned projectiles. J. Spacecr. Rocket **38**(4), 542–549 (2001)
5. Silton, S.I.: Navier–Stokes computation for a spinning projectile from subsonic to supersonic speeds. J. Spacecr. Rocket **42**(2), 223–230 (2005)
6. DeSpirito, J., Heavey, K.R.: CFD Computation of magnus moment and roll damping moment of a spinning projectile. In: AIAA Atmospheric Flight Mechanics Conference and Exhibit, Rhode Island, USA, AIAA 2004-4713 (2014)
7. DeSpirito, J., Plostins, P.: CFD Prediction of M910 projectile aerodynamics: unsteady wake effect on magnus moment. In: AIAA Atmospheric Flight Mechanics Conference and Exhibit, South Carolina, USA, AIAA 2007-6580 (2007)
8. DeSpirito, J.: CFD prediction of magnus effect in subsonic to supersonic flight. In: 46th AIAA Aerospace Sciences Meeting and Exhibit, Nevada, USA, AIAA 2008-427 (2008)
9. Silton, S.I., Dinavahi, S.P.G.: Base drag considerations on a 0.50-caliber spinning projectile. In: 26th AIAA Applied Aerodynamics Conference, Hawaii, USA, AIAA 2008-6739 (2008)
10. De Spirito, J.: Effects of base shape on spin stabilized projectile aerodynamics. In: 26th AIAA Applied Aerodynamics Conference, Hawaii, USA, AIAA 2008-6738 (2008)
11. Sturek, W.B., Mylin, D.C.: Magnus effect on boattailed shell at supersonic speeds. In: AIAA Atmospheric Flight Mechanics Conference, New Mexico, USA, AIAA 81-1900 (1981)
12. Wang, H., Wang, Z., Sun, M., Qin, N.: Large eddy simulation of a hydrogen-fueled scramjet combustor with dual cavity. Acta Astronaut. **108**, 119–128 (2015)
13. Sun, M., Wang, Z., Liang, J., Geng, H.: Flame characteristics in supersonic combustor with hydrogen injection upstream of cavity flameholder. J. Propul. Power **24**(2), 688–696 (2008)
14. Huang, W., Liu, W., Li, S., Xia, Z., Liu, J., Wang, Z.: Influences of the turbulence model and the slot width on the transverse slot injection flow field in supersonic flows. Acta Astronaut. **73**, 1–9 (2012)
15. Simon, F., Decky, S., Guillen, P.: Numerical simulations of projectile base flow. In: 44nd AIAA Aerospace Sciences Meeting and Exhibit Conference, Nevada, USA, AIAA 2006-1116 (2006)
16. Mcdaniel, M., Riddle, D.: Boattail improvements for missile DATCOM. In: 47th AIAA Aerospace Sciences Meeting Including the New Horizons Forum & Aerospace Exposition, Florida, USA, AIAA 2009-908 (2009)
17. Kalatt, D., Hruschka, R., Leopold, F.: Numerical and experimental investigation of the magnus effect in supersonic flows. In: 30th Applied Aerodynamics Conference, New Orleans, Louisiana, USA, AIAA 2012-3230 (2012)
18. Lei, J., Zhang, J., Tan, Z.: Influence of boattail on the magnus effect of spinning non-finned projectile at small angles of attack. Acta Armamentarii **38**(9), 1705–1715 (2017)
19. Deck, S.: Recent improvements in the Zonal Detached Eddy Simulation (ZDES) formulation. Theoret. Comput. Fluid Dyn. **26**(6), 523–550 (2012)
20. Ma, J., Huang, Z., Chen, Z., Xue, D.: Flow separation control of two kinds of microvortex generators for a supersonic spinning projectile. J. Mech. Sci. Technol. **31**(1), 197–205 (2017)

21. Obeid, Q., AlQadi, I., AlMutairi, J.: Investigation of asymmetric flow past a slender body at high angles of attack. Theoret. Comput. Fluid Dyn. **33**, 481–508 (2019)